ORIGINAL ARTICLE

Sustainable manufacturing of maraging steel seamless tube via flow forming: structure–property relations

Amborish Banerjee[1] · Kyle Nelson[1] · David Milliken[2] · Laurie da Silva[1]

Received: 29 January 2025 / Revised: 1 April 2025 / Accepted: 4 April 2025
© The Author(s) 2025

Abstract
Sustainability in manufacturing is increasingly pushing the metal forming sector to manufacture components with less material wastage. Flow-forming is a sustainable manufacturing route to produce high-value near-net-shape components of complex geometries. The triaxial stress-state and localised deformation occurring during this process necessitates the comprehension of underlying deformation micromechanisms. In this study, flow-forming of MLX®19 maraging steel alloy was performed at varying feed rates and the effect on the concomitant microstructural evolution was examined. Increasing the feed rates from 5 to 10 mm/rev resulted in a localised deformation and defects in the flow-formed component. The microstructural features of the outer region of the flow-formed component demonstrated refined and elongated grains while the centre and inner regions exhibited less refined grains. The obtained microstructural heterogeneity was further correlated with the associated governing factors such as the deformation and thermal gradients, as well as strain distribution. Regarding the crystallographic texture evolution, the outer region showed the highest volume fraction (~ 16%) of the rotated Goss component $(011)\left[0\overline{1}1\right]$ indicating that this region underwent excessive shear deformation in addition to compression. On the other hand, the inner region displayed predominant copper-like $(111)\left[0\overline{1}1\right]$ and rotated cube $(001)\left[\overline{1}10\right]$ textures (~ 24.5 and 13.6% respectively) suggesting the fact that the inner region experienced predominantly compressive deformation. Tensile tests confirmed that the flow-formed component demonstrated higher strength and lower ductility compared to the base metal (BM) which was attributed to the dislocation density and refined grain formation.

Keywords Maraging steel · Flow-forming · Mechanical properties · Texture · Fractography

1 Introduction

Industrial globalisation has compelled the manufacturing sector to focus on sustainable manufacturing due to various factors such as depletion of non-renewable resources, global warming, minimising materials wastage, etc. [1]. Sustainable manufacturing aims to design efficient manufacturing processes that lead to superior end product with minimal material wastage thereby reducing carbon emission [2]. Due to the constant exploitation of the environment followed by the enduring depletion of natural resources, fabricating products via sustainable methods in the manufacturing sector is gaining significant attention [3]. Cylindrical components are widely used in aviation, defence, and automobile sectors such as missile tubes, landing gear components, transmission shafts, etc. and, therefore, efficient methods are required to fabricate them. For critical applications, these components

https://doi.org/10.1007/s43452-025-01199-2

Published online: 23 April 2025

are typically fabricated from the machining of large-forged billets, which leads to excessive wastage of material. Therefore, it is vital to identify potential alternative routes to fabricate these components.

Flow-forming is an incremental metal-forming process to fabricate seamless tubes of varying wall thicknesses. Due to its cold work deformation history, it is also considered as an efficient sustainable manufacturing process. The main advantages of this process include reduction in material wastage, attaining accurate profiles with control over material thickness, higher strength than extruded tubes due to more refined grains, lower forming load because of localised deformation, and many others [4]. Though there are various methods to manufacture seamless tubes such as extrusion, rotary piercing, radial forging, etc., the material wastage during these processes results in a poor buy-to-fly ratio (~ 20:1) thereby, increasing the manufacturing cost [5]. Moreover, tubes with very thin (~ 1–5 mm) and varying wall thickness cannot be economically produced by these methods. In contrary, superior mechanical properties and controlled microstructures are obtained via the flow-forming process [6]. MLX®19 is a new grade of precipitate-hardened alloy which is used for aerospace, defence, and automobile sectors due to its high corrosion resistance. MLX®19 belongs to a class of ultrahigh strength low-carbon martensitic steels which are characterized by the presence of intermetallic precipitates. These nano-precipitates are accountable for increasing the strength of the material without much loss in ductility [7]. Therefore, flow-forming of MLX®19 is a prospective fabrication method to create hollow cylindrical sections. Moreover, due to the complex stress state throughout the metal forming process, it is equally important to examine the concomitant microstructural features and texture evolution during the flow-forming of MLX®19 alloy to further tailor the mechanical properties.

To date, despite extensive studies on the flow-forming of various steels, predicting optimized flow-forming parameters and establishing structure–property relations for maraging steel remains scarce. For instance, Razani et al. [8] investigated the effect of mandrel speed and feed rate on the hardness evolution of flow-formed AISI 321 steel by developing a mathematical model using the response surface methodology (RSM). The model predicted that material hardness increases with rising mandrel speed and decreases with a deteriorating feed rate. Tsivoulas et al. [9] investigated the influences of four flow-forming parameters viz. feed rate, roller contact angle, thickness reduction, and hardness on the residual stress generation in Cr–Mo–V steel ferritic steel tubes. The authors found that high feed rate and low contact angle rollers were preferred to maintain low residual stresses. Shinde et al. [10] evaluated the influence of the roller tip radius and the friction at the roller-workpiece interface on the flow-forming behaviour of maraging steel by developing a 3D finite element model. The authors reported an increase in the ineffective plastic stress with an increase in the feed rate. Karakas et al. [11] established the structure–property correlations of flow-formed AISI 5140 steel by performing forming trials at ~ 50% reduction ratio. The authors observed a substantial increase in the strength and hardness of the formed material, accompanied by a severe drop in ductility, which was attributed to dislocation generation and their pile-up during the forming process. Roy et al. [12] investigated the influence of mandrel speed, roller geometry and thickness reduction on the evolution of equivalent plastic strain in AISI 1020 steel during the flow forming process by micro-indentation hardness tests. It was reported that the material exhibited an increase in the plastic strain near the mandrel with higher forming passes. Guillot et al. [13] carried out shear forming of 304L stainless steel and reported the transformation of equiaxed grains into elongated grains along with shear band formation during the process. The authors further analysed the crystallographic texture evolution and found shear to be the dominant deformation mode. Podder et al. [14] investigated the effects of different heat treatments (HTs) namely annealing, spheroidising, and tempering on the mechanical properties of flow-formed AISI4340 steel. The authors reported spheroidising as the most favourable HT technique due to the presence of globular secondary phases. Similarly, Maj et al. [15] investigated the flow-forming behaviour of martensitic stainless steel 17–4 PH by conducting forming trials at four different strains followed by ageing. The authors observed that increased strain (i.e., thickness reduction) resulted in an increase in ultimate strength (~ 400 MPa), accompanied by a ~ 15% decrease in the ductility compared to the as-received condition. Further examination of the microstructure revealed evidence of strain hardening in the form of dense forest dislocations.

Based on the extensive literature survey, it is noteworthy that limited studies are available on the flow-forming behaviour of MLX®19 maraging steel. Therefore, to answer the aforementioned scarcity of research studies, the micro-mechanisms of plastic deformation during the flow-forming of MLX®19 was investigated in this paper. Preforms in the form of cylindrical tubes were flow-formed at three different feed rates and their effect on the formability of MLX®19 was investigated. The concomitant microstructural features and crystallographic texture were characterised and methodically correlated with the deformation behaviour.

2 Experimental procedure

In this study, MLX®19 steel in its as-received state (solution heat treated) was machined to form preforms measuring 110 mm in length and 82.5 mm in outer diameter with a wall thickness of 15 mm. Amongst various critical parameters obtained from previous research investigations [9–11], the impact of roller feed rate on the deformation behaviour of MLX®19 alloy was investigated in this study. Three flow-forming trials (presented in Table 1) were executed using the VUD 600 vertical flow-former machine, the schematic is shown in Fig. 2a. The parameters were determined using an in-house analytical model based on the upper bound theorem, and details of the model have been published elsewhere [16]. Note that due to the proprietary information, scaled parameters have been provided in Table 1. The two rollers and mandrel of the VUD 600 machine are denoted by R_1, R_2 and M, respectively. In all three forming trials, the feed rate which is considered as the most critical process parameter was adjusted within the range of 5–10 mm/rev, while the other parameters as such roller attack angle, roller tip radius, spindle speed, and roller gaps remained constant. Given the initial wall thickness of 15 mm, a greater reduction per pass is typically necessary to facilitate axial movement of the material and avoid stagnation of material flow near the mandrel. Therefore, the desired final wall thickness of ~ 9 mm (from the initial 15 mm) was achieved through three consecutive passes, each reducing the thickness by ~ 2 mm in a single pass. Coolant (Hocut 4260) was used during all the forming trials to dissipate the heat generated in the formed component.

The mechanical properties and the concomitant microstructural evolution of the flow-formed components were characterised to establish the process-structure–property relationships. The cross-sectional macro-slices from the optimum flow-formed component (discussed later) were extracted parallel to the axial length as shown in Fig. 1b and then mounted for metallurgical investigation. The metallographic specimens were prepared (i.e. grinding and polishing) according to the ASTM E-11 standard [17] and then etched using Vilella's reagent (100 ml ethanol + 5 ml HCL + 1 gm picric acid). The etched specimens were examined under the Leica DM6000 M optical microscope (OM) and FEI QuantaTM 250 field emission gun (FEG) scanning electron microscope (SEM) to examine the microstructural features. The mechanical properties were investigated by performing the hardness measurement, and uniaxial tensile tests. The microhardness maps across the various regions of flow-formed component (outer surface, centre, and inner surface) were constructed using a Struers Vickers microhardness indentation testing machine by applying a load of 200 gf for 12 s. On average, more than 500 hardness measuring points were collected and processed for constructing the hardness profile for each flow-formed component. The strength and ductility of the flow-formed components were predicted by performing uniaxial tensile tests on a screw-driven Zwick Z250/SW5A testing machine calibrated with a 250 kN load cell. The machine was controlled using test Xpert®II software to record the raw data which was post-processed to calculate the mechanical properties. The tensile tests were conducted at ambient temperature under an engineering strain rate of 10^{-3}/s as per the ASTM E-8 M standard [18]. Moreover, three tests were conducted to confirm the repeatability of the obtained results. For the tensile test, round specimens with 10 mm gauge length and 2.5 mm diameter were extracted

Table 1 Parameter setup used for flow-forming MLX®19

Run	Attack angle	Feed rate (mm/rev)	Total passes	Reduction pass (mm)
FF-1	25	5	3	2
FF-2	25	7.5	3	2
FF-3	25	10	3	2

 https://doi.org/10.1007/s43452-025-01199-2

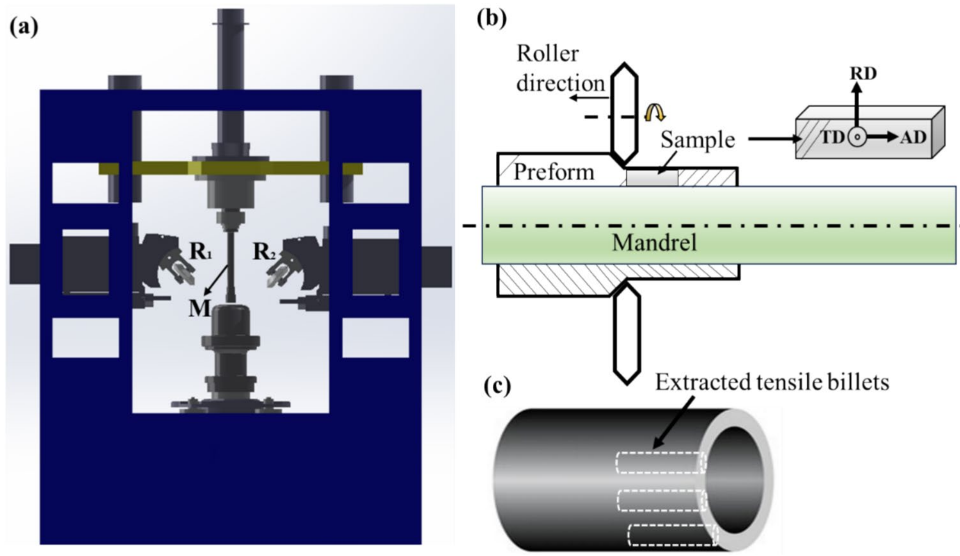

Fig. 1 Schematic representation of the (**a**) VUD 600 machine where R_1, R_2 and M represent the lead roller, finishing roller, and mandrel, respectively, **b** roller-preform interaction and sample extraction, and **c** extraction of tensile billets in the radial direction of the flow-formed component

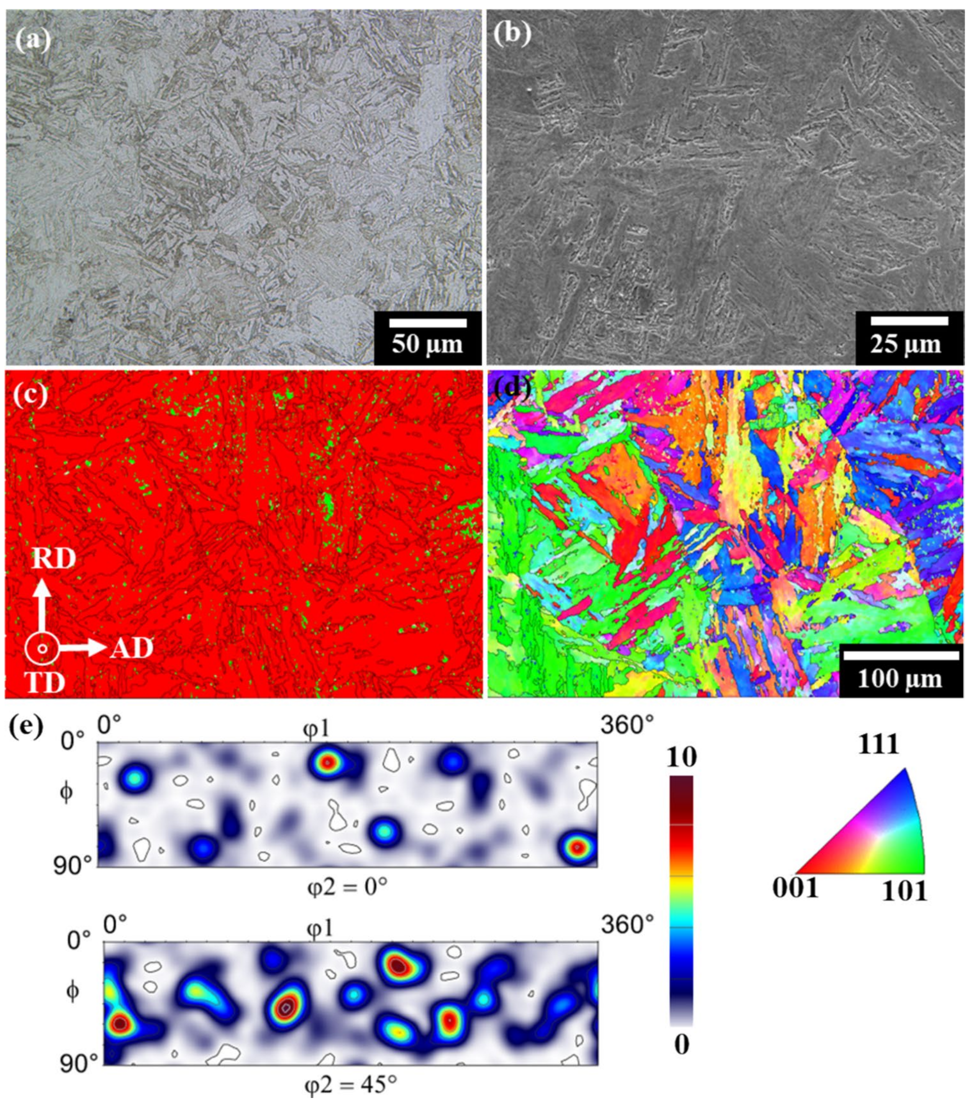

Fig. 2 **a** OM and (**b**) SEM images of the as-received material in the solution heat-treated condition, **c** EBSD phase map and (**d**) IPF of the as-received material along with the super-imposed HAGBs, **e** the $\varphi = 0$ and 45-degree ODF sections of the BCC phase showing random texture distribution

from the flow-formed component in the axial direction, as shown in Fig. 2c. The strain was measured using an axial clip-on extensometer. The fracture surface of the failed specimens was examined under the SEM to find the concomitant changes in the microstructures and to predict the micro-mechanisms leading to the failure of the material. The EBSD patterns were collected by tilting the sample to 70° at an accelerating voltage of 20 kV and the scans were performed with a step size of 0.1 µm at 5 × 5 binning mode. For EBSD scans, the specimens were ground and then vibro-polished for 12 h using OPS suspension. The post-processing of the obtained data was performed using the Aztec crystal and Atex 5 software [19].

3 Results and discussion

3.1 Initial microstructure

The initial microstructure of the as-received material in the solution heat-treated condition is shown in Fig. 2. As evident from the OM (Fig. 2a) and SEM (Fig. 2b) images, the material exhibited a typical lath martensitic structure with an average measured hardness ~ 350 HV. The phase map with superimposed high-angle grain boundaries (θ > 15 degrees) and the inverse pole figure (IPF) map shown in Fig. 2c and d, respectively, reveal the orientation of martensitic laths on various crystallographic planes. From the phase map (red for martensite and green for retained austenite), it is evident that traces of retained austenite (~ 3%) were also found in the as-received material. The corresponding $\varphi = 0$ and 45° sections of the orientation distribution function (ODF) map in Fig. 2e illustrated a heterogeneous texture with some random orientation. These textures were likely to be developed during the forging and solution heat-treatment processes.

3.2 Effect of feed rate

The flow-formed components corresponding to three different roller feed rates viz. 5, 7.5 and 10 mm/rev are shown in Fig. 3a–c respectively, and as evident, a decrease in the fish-scaling was observed with increasing feed rate. Fish scaling is observed when the material during the flow-forming process is subjected to lower feed rates [20]. During the flow-forming process, the material is subjected to a complex stress-state and experiences three

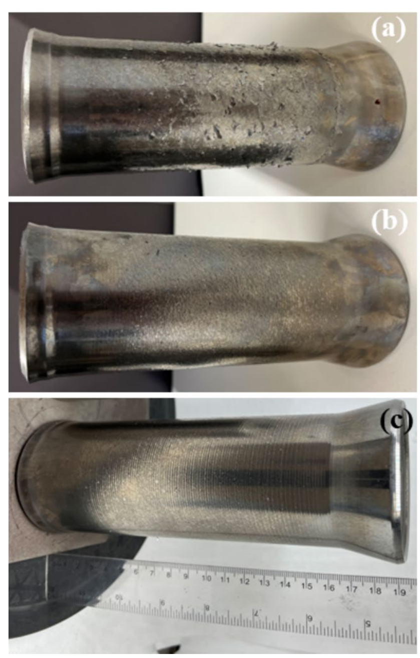

Fig. 3 The flow-formed components obtained from the preform at different feed rates of (**a**) 5 mm/rev, **b** 7.5 mm/rev, and **c** 10 mm/rev

different forces viz. the radial, axial and circumferential forces. The radial force (F_r) acts in the outward horizontal direction and is responsible for the subsequent compression and deformation of the material in the radial direction. The circumferential force (F_θ) acts in a tangent direction to the workpiece circumference and provides twisting to the material, this force is generally minimum. On the other hand, the axial force (F_a) acts along the longitudinal (i.e. vertical) direction and leads to the elongation of tube material in addition to the desired shape. In general, lower feed rates lead to slower movement of the material ahead of the rollers thus, resulting in an inadequate material flow to uniformly fill the entire deformation zone. In other words, the contact area and deformation zone are narrow at lower feed rates. Therefore, certain regions of the material experience excessive strain, leading to irregular deformation patterns reminiscent of fish scales. This defect can be mitigated by increasing the feed rate to ensure sufficient metal flow and uniform distribution in the deformation zone. This is evident from Fig. 3b and c, which show a decrease in the fish-scale morphology with increasing feed rate from 5 to 7.5 and 10 mm/rev, respectively. Increased feed rates also aid in reducing the cycles required to traverse the deformation zone in flow forming thereby, decreasing the cyclic loading experienced by the material. This reduction in cyclic loading helps in enhancing the fatigue resistance and dimensional accuracy of the formed parts. Another feature associated with higher feed rates is the increase in the surface roughness. Though in this study the surface roughness was not measured, qualitatively an increase in the roughness (circumferential marks) was observed as evident from Fig. 3a–c. According to Ebrahimi et al. [21], increasing feed rates lead to higher longitudinal movement of the roller along the tube component. Therefore, even though the material stays under the roller for a comparatively shorter time and swiftly exists the deformation zone, the contact surface between roller and material increases for a single revolution which finally leads to an increase in the surface roughness. Moreover, according to Rajan et al. [22], increasing the feed rate leads to an increase in the radial force and this parameter also plays a vital role in increasing the surface roughness of the formed component. Similar results on the surface roughness have been reported earlier by other researchers [23, 24].

3.3 Microstructural evolution and deformation micromechanisms

The cross-section microstructures across different regions of the flow-formed component are shown in Fig. 4. Based on the concomitant microstructural features, the outer region was classified as a severe plastic deformation zone (SPDZ), while the centre and inner regions were classified as less plastically deformed zone (LPDZ). The microstructure of the outer region shown in Fig. 4a exhibited fibrous structure with elongated and refined grains oriented along the axial direction (material flow), while the centre region shown in Fig. 4b illustrated grains that were less elongated and less refined compared to those in the outer region. The inner region (Fig. 4c), in contrast, exhibited coarser grains with less preferred orientation in the axial direction. This observed heterogeneity in the microstructure across different regions can be associated with various governing factors experienced by the material during the flow-forming process as such (a) deformation gradient, (b) strain distribution, (c) thermal gradient and cooling rate, (d) strain rate, etc.

In general, during the flow-forming process, the outer region of the material is in direct contact with the forming tool (i.e. rollers), whereas the centre and inner regions are not in direct contact with the rollers. Therefore, it is expected that the outer surface will be subjected to comparatively higher deformation than the centre and inner regions. This results in a negative deformation gradient from the outer to the inner region of the component in addition to an uneven strain distribution. Both these factors significantly contribute to the formation of elongated and more refined grains in the outer region. Cooling rate is another critical governing factor in altering the grain growth and transformation kinetics of the material. Since the outer regime experiences more deformation and strain, significantly higher amount of heat is generated at the outer regime due to mechanical work. This additional heat results in faster cooling rates at the outer surface as it facilitates rapid heat dissipation. Moreover, since the centre and inner regions are not in direct contact with the rollers during the forming process, these regions experience comparatively less efficient heat dissipation than the outer region. Thus, a thermal gradient is established with higher and lower cooling rates at the outer and inner regions, respectively. This further leads to

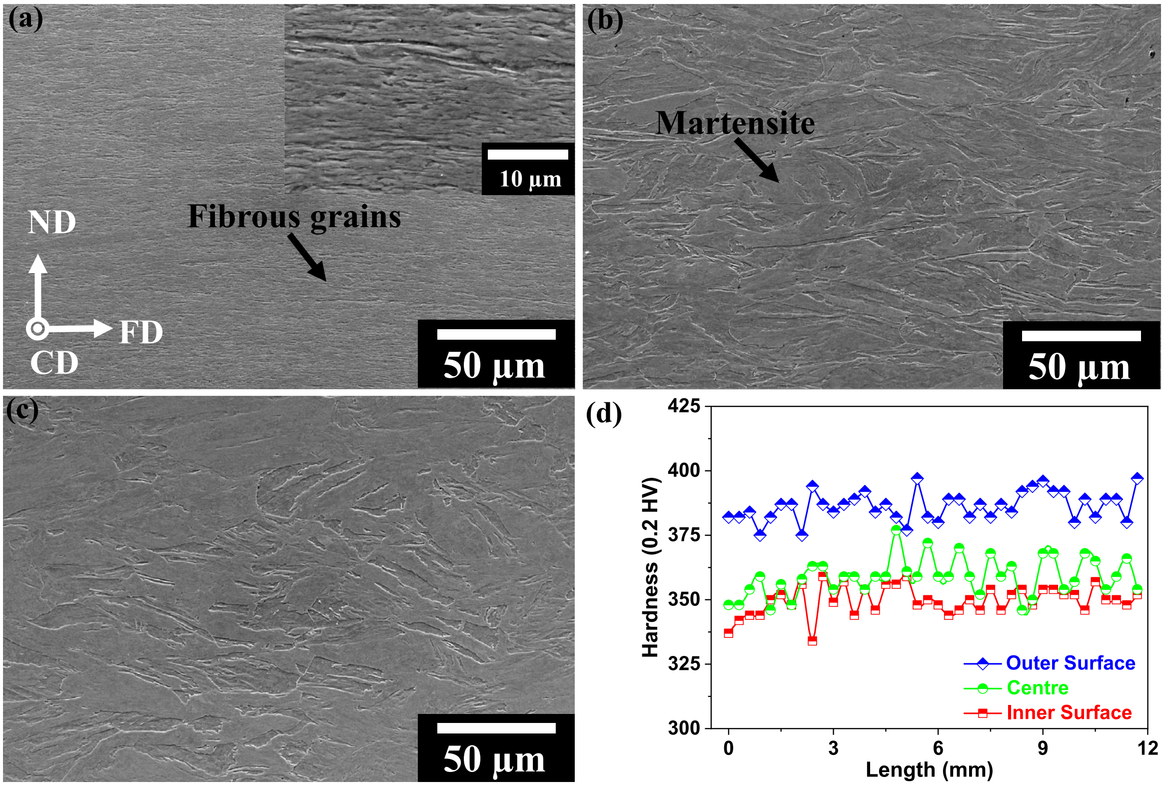

Fig. 4 SEM images of the formed material (**a**) outer regime exhibiting elongated and fibrous grains, **b** and **c** showing the centre and inner regimes respectively, with presence of coarse microstructures

different microstructural features with the presence of fine grains at the outer regime and coarse microstructures in the centre and inner regions. Furthermore, surface boundary conditions of the material play a crucial role in heat transfer. In flow-forming, while the outer surface is exposed to ambient air or a moving air stream, the inner surface remains in direct contact with the metallic mandrel. This contrast in thermal environments results in varying heat dissipation rates, which play a crucial role in shaping the grain structure and contributing to the differences in microstructural evolution across the material. These observations were also reflected in the hardness profile shown in Fig. 4d which demonstrates the highest average hardness (~385 HV) at the outer region due to finer grains. This was followed by an overall decrease in the average hardness at the centre and inner regions due to coarse microstructures. The matrix exhibited no strain-induced porosities or cracks across the length and thickness regions which further indicates the efficiency of the flow-forming process in manufacturing defect-free parts. In general, strain-induced porosities are voids or pores that develop within the material due to the plastic deformation and strain encountered during the metal-forming processes. These porosities can have a significant influence on the mechanical properties and overall quality of the formed component.

3.4 EBSD investigation

The inverse pole figure (IPF) maps of the outer and inner regions of the flow-formed workpiece (after the final reduction in thickness) along with the grain distribution histograms are shown in Fig. 5. The IPF map of the outer region (SPDZ) shown in Fig. 5a exhibited a flattened ribbon-like morphology. This is more evident from the magnified image (Fig. 5b) where the elongated grains are observed to be oriented in the axial/ forming direction. During flow-forming, a finite amount of the material is expected to get piled up in front of the rollers. This material initially experiences radial tensile strain followed by compressive strain in the same direction once the

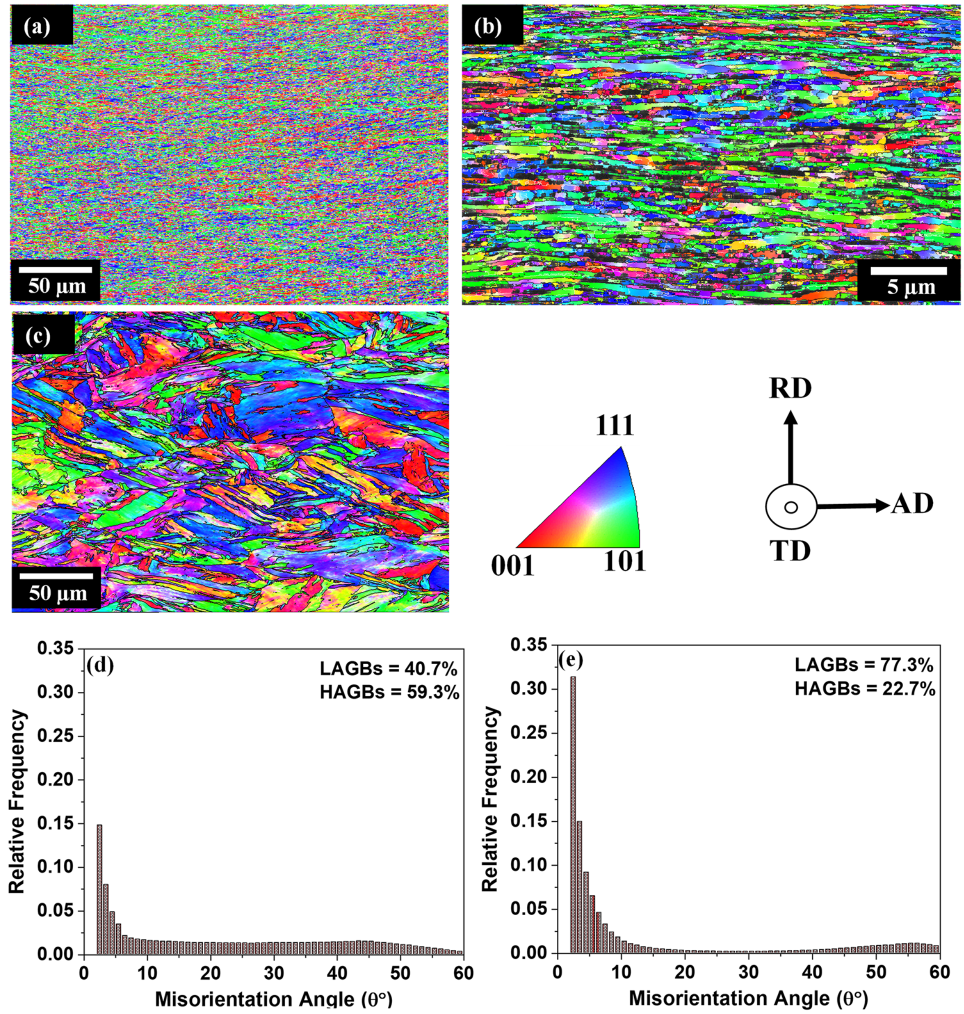

Fig. 5 **a** IPF image depicting (**a**) the formation of refined grains in the outer region of the flow-formed component, **b** higher magnified image showing the elongated grains oriented in the axial direction, **c** IPF image of the inner region showing comparatively coarser grains, **d** and **e** showing the grain boundaries volume fraction of the outer and inner regimes, respectively

rollers pass [25]. Moreover, since the workpiece is subjected to an angular motion and is constantly compressed by the rollers, shear stresses and strains are generated which leads to the plastic deformation. This complex stress state and heterogeneous deformation resulted in the fragmentation of martensitic microstructure into ultra-refined grains, as earlier reported by Miura et al. [26]. The calculated grain size based on the ECD (equivalent diameter) approach was calculated ~ 1.9 µm. On the other hand, comparatively coarser microstructure was observed in the inner region (LPDZ) with the average grain size measured ~ 23.7 µm. This is due to the fact that the rollers were not in direct contact, and the deformation was not that intense. Note that due to very refined grains, the IPF map of the outer region (Fig. 5a) is provided without any grain boundaries whereas, the magnified image shown in Fig. 5b and the IPF of the inner region (Fig. 5c) consists of high angle grain boundaries (HAGBs, $\theta > 15°$).

The misorientation angle distributions for the outer and inner regions are presented in Fig. 5d and e, respectively. The volume fractions of the HAGBs at the outer and inner regions were calculated ~ 59.3 and 22.7%, respectively. During the initial stage/reduction pass of the cold flow-forming process, the strain-hardening phenomenon is characterised by the generation of a large number of dislocations within the grains. These dislocations further rearrange themselves inside the grains, leading to the formation of subgrain structures. These subgrains having low misorientations ($\theta < 15°$), also described as low-angle grain boundaries (LAGBs), are responsible for the strength of the material due to the restricted movement of dislocations. However, with the ongoing deformation, it is expected that the subgrains may rotate and coalesce thereby increasing the misorientation between the adjacent subgrains. Once the misorientation exceeds the threshold value (15°), the LAGBs are transformed into HAGBs, and the grains are oriented in the deformation (or axial) direction. This phenomenon was reflected in the IPF maps (Fig. 5a, b) and chart (Fig. 5d) where elongated grains were observed in the axial direction along with a higher volume fraction of HAGBs at the outer region than the inner region. It is worth mentioning here that though dynamic recrystallisation leads to an increase in the HAGBs, this phenomenon was not considered as the temperature during the cold flow-forming was much below the recrystallisation temperature of MLX®19 (~ 687 °C) [27].

From the SEM and EBSD analyses, it can be inferred that a heterogeneous microstructure existed across the thickness direction. These observed microstructural features can be attributed to the (a) triaxial stress-state, and (b) localised non-uniform stress field. According to Wang et al. [28], the triaxial stresses are mainly developed at the roller-workpiece contact area and to accommodate these stresses, it is expected that the grains will bend over in the axial direction. The localised non-uniform stress field above and below the rollers may also result in the formation of elongated grains, this has been manifested in the microstructures shown in Fig. 4a and 5b. The matrix exhibited no strain-induced porosities or cracks across the length and thickness regions which further indicates the efficiency of the flow-forming process in manufacturing defect-free parts. Moreover, no shear bands across the thickness were noticed. The higher hardness at the outer region in comparison to the centre and inner regions can be correlated to the higher grain refinement due to severe deformation which is in agreement with the Hall–Petch strengthening law [29].

3.5 Deformation crystallographic texture evolution

It is well understood from previous studies [27, 30], that analysing the crystallographic texture evolution helps in determining the predominant deformation mechanisms and also influences the mechanical performance of the material. As mentioned earlier, the material during flow-forming is subjected to both compressive and shear loads. However, the variations in microstructural features across the wall thickness of the formed component suggest different deformation modes may occur at the outer and inner regions of the formed tube. To explore this, the orientation distribution function (ODF) sections obtained from the large area EBSD maps were plotted to identify the dominant deformation textures. The ODF sections corresponding to the outer and inner regions of the formed component along with the evolved rolling texture components at $\varphi_1 = 0°$ and 45° sections are shown in Fig. 6. The ODF sections of the outer region corresponding to $\varphi_2 = 0°$ and 45° are shown in Fig. 6a, while the calculated volume fractions of the prominent rolling textures are presented in Fig. 6c. As evident, a significant change in the maximum texture intensity was observed with the lowest intensity being exhibited by the outer region. This further suggests that the deformation in the outer region was much severe than in the inner region, therefore resulting in the formation of new grains with new orientations. The ideal rolling and shear texture components in BCC metals are presented in Table 2. As observed, amongst the ideal rolling texture components, the z—rotated Goss component $(011)\left[0\bar{1}1\right]$ and a_3- copper-like texture $(111)\left[0\bar{1}1\right]$ of γ-fiber exhibited the highest volume fractions of 16 and 12.9%, respectively. Though additional texture components i.e. a_2 (211)[011], a_1—rotated cube $(001)\left[\bar{1}10\right]$ of θ-fiber, and g_1 $(011)\left[0\bar{1}1\right]$ of the γ-fiber were also observed, their intensities were comparatively weaker with low volume fractions. In general, the regular Goss texture is not stable during the plane strain deformation typically due to the change in the strain path [31]. This further leads to the rotation of regular Goss texture, thereby resulting in the formation of rotated Goss texture. Similarly, the development of copper-like texture is common during specific deformation processes where grains with new orientations are generated due to the applied stress. In contrast, for the inner region of the formed component as shown in Fig. 6b and d, the a_3—copper-like $(111)\left[0\bar{1}1\right]$ and a_2 (211)[011] components emerged as the prominent texture components with calculated volume fractions of 24.5 and 13.6%, respectively. Moreover, weak rotated Goss $(011)\left[0\bar{1}1\right]$ and rotated cube $(001)\left[\bar{1}10\right]$ components were also found, each with a computed volume fraction of ~ 6.5%.

From the reported results, it is evident that the rotated Goss component exhibited the highest volume fraction in the outer region of the formed component compared to the inner region. Previous studies [31–33]

 https://doi.org/10.1007/s43452-025-01199-2

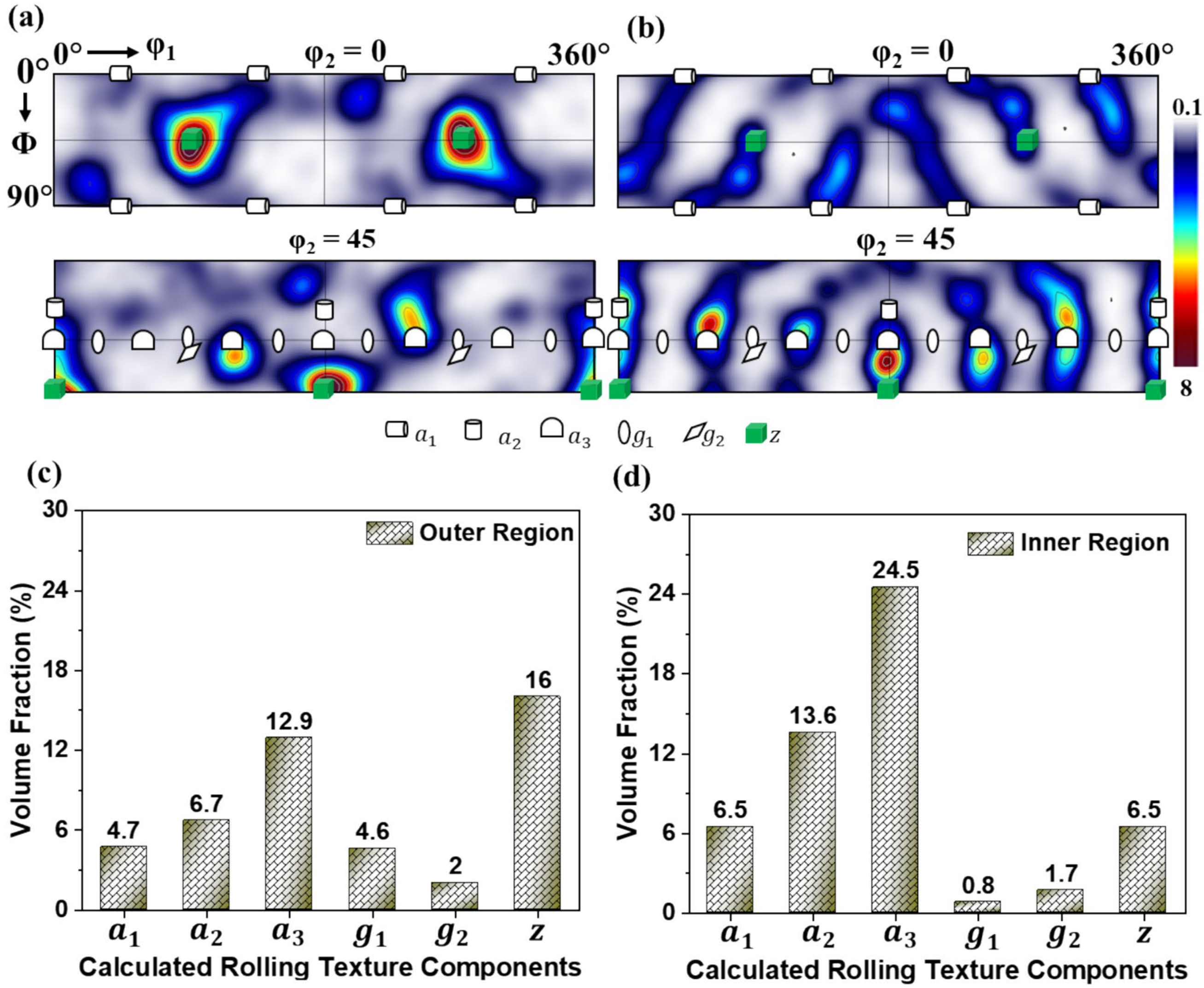

Fig. 6 $\varphi_2 = 0$ and 45° ODF sections of the flow-formed component (BCC phase) along with the superimposed rolling texture components of (**a**) outer region and (**b**) inner region, calculated volume fraction of the texture components of the (**c**) outer region and (**d**) inner region

indicate that severe shear deformation leads to the formation of the rotated Goss texture in BCC metals. This is likely due to the alignment of planes and < 011 > directions along the shear direction. In contrast, the copper and rotated cube components are less prominent during predominant shear deformation and are typically observed during predominant compression deformation. These findings suggest that the outer region of the formed component experienced more shear deformation than the inner region. To further concrete this argument, the ideal shear texture components were superimposed on the $\varphi_2 = 0°$ and 45° ODF sections of the outer and inner regions of the flow-formed component as shown in Fig. 7a and b. The total volume fraction of the shear texture components corresponding to the outer and inner regions were calculated ~ 14.6 and 8.3% (see Fig. 7c and d), respectively. This indicates that, although compression was the major deformation mode, the outer surface of the formed component experienced significantly higher shear deformation than the inner surface. These findings were found in agreement with previous results reported on the flow-forming of Cr–Mo–V steel tubes by Tsivoulas et al. [9, 34].

Table 2 Ideal rolling and shear texture components formed during the plastic deformation in metals with BCC crystal structures, reported by [35]

Deformation mode	Texture components	Miller indices $(hkl)[uvw]$	Euler angles (°) φ_1, φ, φ_2
Rolling	a_1–Rotated cube	$(001)[110]$	0, 0, 45
	a_2	$(112)[1\bar{1}0]$	0, 35.26, 45
	a_3	$(111)[0\bar{1}1]$	0/60, 54.74, 45
	g_1	$(111)[1\bar{2}1]$	30, 54.74, 45
	g_2	$(111)[\bar{1}\bar{1}2]$	90, 54.74, 45
	z- Rotated Goss	$(110)[110]$	
Shear	D_1	$(11\bar{2})[111]$	270, 35, 35
	D_2	$(\bar{1}\bar{1}2)[111]$	90, 35, 45
	E_1	$(01\bar{1})[111]$	(145, 90, 45), (325, 90, 45)
	E_2	$(0\bar{1}1)[111]$	(35, 90, 45), (215, 90, 45)
	J_1	$(0\bar{1}1)[\bar{2}11]$	(125, 90, 45), (305, 90, 45)
	J_2	$(1\bar{1}0)[\bar{1}\bar{1}2]$	(55, 90, 45), (235, 90, 45)
	F	$(1\bar{1}0)[\bar{1}\bar{1}2]$	(90, 90, 45), (270, 90, 45)

3.6 Mechanical characterisation and fracture surface examination

The engineering stress–strain curves of the MLX®19 alloy in both as-received (solution-treated) and formed conditions are shown in Fig. 8. It is evident that, compared to the solution-treated condition, the formed material exhibited an increase in ultimate strength. The ultimate strength values in the received condition and after flow-forming were calculated ~ 1030 and 1159 MPa, respectively. This increase in strength can be attributed to the formation of refined grains. According to the Hall–Petch relationship [29], a reduction in the grain size leads to an increase in the strength of a material which is reflected in the stress–strain curve of the formed component. However, smaller grains generated during the forming process also introduce additional grain boundaries which restrict the dislocation motion thereby, limiting the ability of the material to deform plastically. This results in a decrease in the ductility of the formed component (~ 5%) as compared to the as-received material which was measured at ~ 17%. The fracture surface of the flow-formed component shown in Fig. 8b exhibited a typical cup and cone fracture along with the presence of both equiaxed and elongated dimples. In general, dimples are formed due to the nucleation, growth, and coalescence of microvoids within the material and are an indication of ductile failure. This indicates that though the flow-formed material exhibited less ductility than the as-received material, the failure mode was predominantly ductile.

4 Conclusions

In this paper, the formability of MLX®19 alloy was investigated by conducting trials at three different feed rates. An analytical in-house model was developed, and the structure–property relations were established. The key findings are summarised as follows:

 https://doi.org/10.1007/s43452-025-01199-2

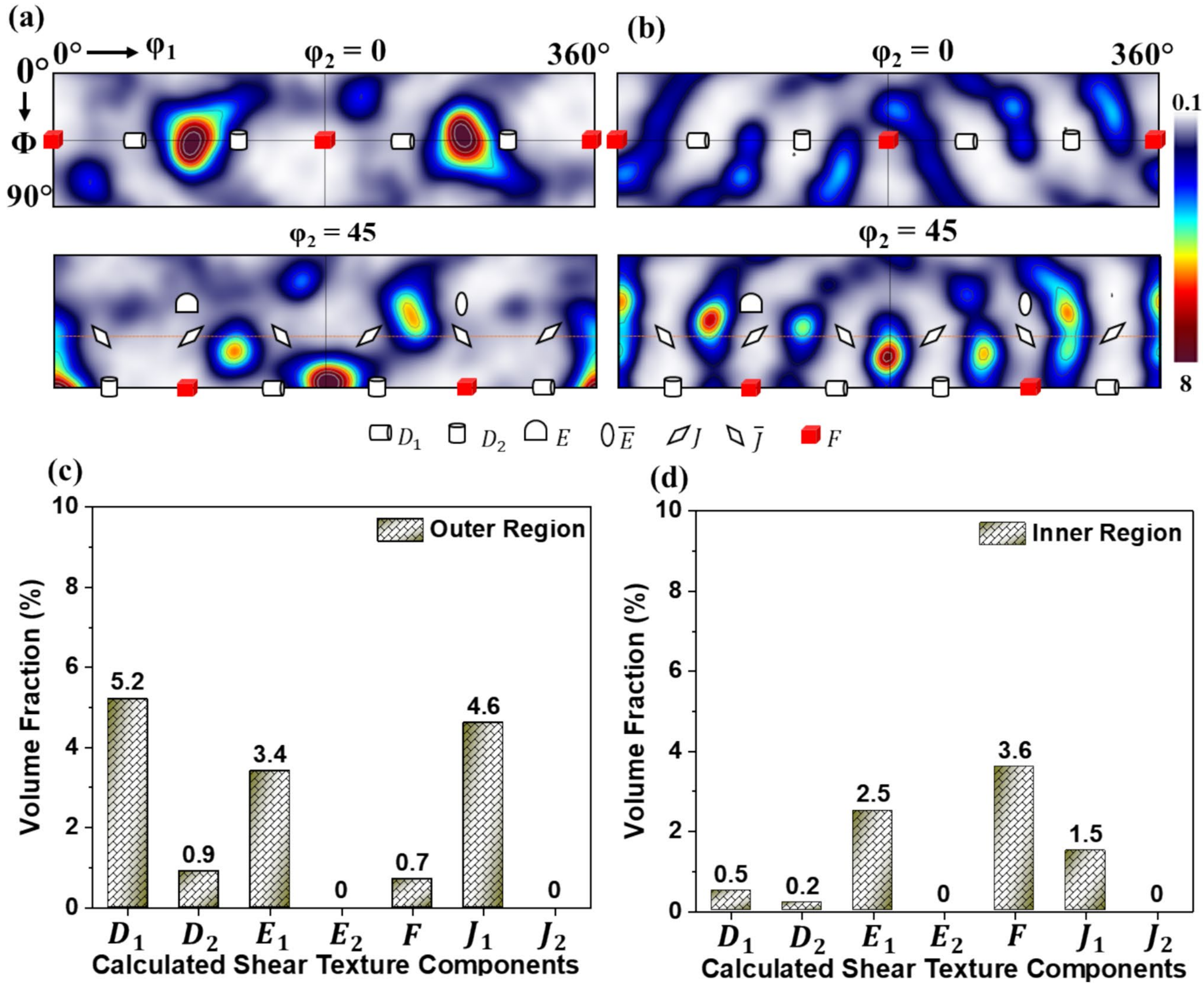

Fig. 7 $\varphi_2 = 0$ and 45° ODF sections of the flow-formed component (BCC phase) along with the superimposed shear texture components of (**a**) outer region and (**b**) inner region, calculated volume fraction of the texture components of the (**c**) outer region and (**d**) inner region

(a) Increasing the feed rates produced a smooth outer surface free of scale-like patterns, whereas decreasing the feed rates led to an increase in the fish-scale formation. This was because the contact area and deformation zone were narrower at lower feed rates, causing excessive strain on the material and resulting in irregular deformation patterns indicative of fish scales. Based on the experimental findings, it was confirmed that the material during flow-forming was subjected to plane strain condition.

(b) The microstructure of the outer region of the flow-formed component exhibited the formation of extremely refined grains with an average grain size ~ 1.9 µm. In contrast, the inner region exhibited a coarser microstructure with an average grain size measured ~ 23.7 µm. This variation in the grain size was also reflected in the hardness measurement, where the highest hardness of ~ 385 HV was measured for the outer region, while the average hardness in the inner region was measured ~ 345 HV. This heterogeneity in microstructure was attributed to the key factors experienced by the material during the flow-forming process, such as deformation gradient, strain distribution, thermal gradient, and strain rate.

(c) The crystallographic texture analysis indicated the highest intensity of rotated Goss $(011)\left[0\overline{1}1\right]$ and copper-like $(111)\left[0\overline{1}1\right]$ components in the outer region of the flow-formed component, with calculated volume frac-

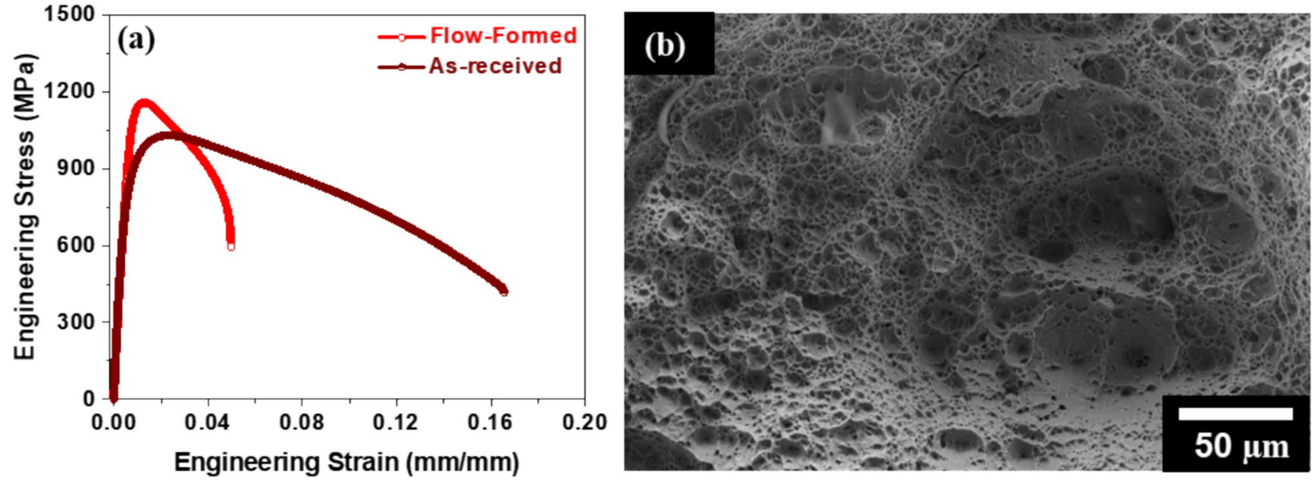

Fig. 8 **a** Engineering stress–strain curves of the as-received and flow-formed components, and **b** fracture surface of the flow-formed component exhibiting dimples

tions of 16% and 12.9%, respectively. In contrast, the inner region exhibited predominant copper-like $(111)\left[0\overline{1}1\right]$ and (211)[011] texture components, with volume fractions of 24.5% and 13.6%, respectively. In general, shear deformation leads to the formation of rotated Goss texture, while the rotated copper and rotated cube components are typically observed during compressive deformation. These observations imply that the outer region of the formed component experienced both shear and compression deformation, while the inner region underwent predominantly compressive deformation. This conclusion is further supported by the volume fractions of shear texture components which were calculated ~ 14.6% and 8.3% for the for the outer and inner regions, respectively.

(d) The flow-formed component exhibited superior strength compared to the as-received material, with ultimate tensile strength values of ~ 1159 MPa and 1030 MPa, respectively. This increase in the strength was attributed to the formation of refined grains, which also led to a decrease in ductility for the formed component (~ 5%) compared to 17% for the as-received material. The fracture surface of the flow-formed component exhibited a typical cup and cone fracture, featuring both equiaxed and elongated dimples.

Acknowledgements The authors would like to acknowledge the support provided by the Advanced Forming Research Centre. Kornelia Kondziolka is acknowledged for preparing the metallurgical specimens and Steven Waugh for conducting the flow-forming. Jacqueline Schramm is acknowledged for conducting the mechanical tests. We also acknowledge the material donation from Aubert & Duval.

Author contributions Amborish Banerjee—Conceptualisation, Date Curation, Formal Analysis, Investigation, Validation, Visualization, Writing original draft, Kyle Nelson—Date Curation, Investigation, Writing, Formal Analysis, David Milliken—Investigation, Formal Analysis, Laurie da Silva—Funding Acquisition, Project Administration, Resources, Supervision.

Funding This project received funding from the UK's High-Value Manufacturing CATAPULT and Tier-1 members of the AFRC.

Data and code availability The data support the findings of this study are available upon reasonable request.

Declarations

Conflict of interest The authors declare that they have no conflict of interest or competing financial interests that have appeared to influence the reported study.

Ethical approval NA.

Open Access This article is licensed under a Creative Commons Attribution 4.0 International License, which permits use, sharing, adaptation, distribution and reproduction in any medium or format, as long as you give appropriate credit to the original author(s) and the source, provide a link to the Creative Commons licence, and indicate if changes were made. The images or other third party material in this article are included in the article's Creative Commons licence, unless indicated otherwise in a credit line to the material. If material is not included in the article's Creative Commons licence and your intended use is not permitted by statutory regulation or exceeds the permitted use, you will need to obtain permission directly from the copyright holder. To view a copy of this licence, visit http://creativecommons.org/licenses/by/4.0/.

References

1. Jayal AD, Badurdeen F, Dillon OW, Jawahir IS. Sustainable manufacturing: Modeling and optimization challenges at the product, process and system levels. CIRP J Manuf Sci Technol. 2010;2(3):144–52.
2. Narayanan RG, Gunasekera JS. Introduction to sustainable manufacturing processes. In: Narayanan RG, Gunasekera JS, editors. sustainable manufacturing processes. Academic Press; 2023. p. 1–28.
3. Choi J-K, Schuessler R, Ising M, Kelley D, Kissock K. A pathway towards sustainable manufacturing for mid-size manufacturers. Procedia CIRP. 2018;69:230–5.
4. Dixit PM, Dixit US. Modeling of metal forming and machining processes: by finite element and soft computing methods. London: Springer; 2008. p. 1–32.
5. McAndrew AR, Alvarez Rosales M, Colegrove PA, Hönnige JR, Ho A, Fayolle R, Eyitayo K, Stan I, Sukrongpang P, Crochemore A, Pinter Z. Interpass rolling of Ti-6Al-4V wire + arc additively manufactured features for microstructural refinement. Addit Manuf. 2018;21:340–9.
6. Cao Z, Wang F, Wan Q, Zhang Z, Jin L, Dong J. Microstructure and mechanical properties of AZ80 magnesium alloy tube fabricated by hot flow forming. Mater Des. 2015;67:64–71.
7. A. Banerjee, L. Da Silva, H. Sharma, A. Platts, S. Rahimi, (2023) Evolution of microstructure in MLX®19 maraging steel during rotary friction welding and finite element modeling of the process. J Manuf Sci Eng. 145(10).
8. Razani NA, Jalali Aghchai A, Mollaei Dariani B. Flow-forming optimization based on hardness of flow-formed AISI321 tube using response surface method. Int J Adv Manuf Technol. 2014;70(5):1463–71.
9. Tsivoulas D, Quinta da Fonseca J, Tuffs M, Preuss M. Effects of flow forming parameters on the development of residual stresses in Cr–Mo–V steel tubes. Mater Sci Eng, A. 2015;624:193–202.
10. Shinde H, Mahajan P, Singh AK, Singh R, Narasimhan K. Process modeling and optimization of the staggered backward flow forming process of maraging steel via finite element simulations. Int J Adv Manuf Technol. 2016;87(5):1851–64.
11. Karakaş A, Kocabıçak AC, Yalçınkaya S, Şahin Y. Flow forming process for annealed AISI 5140 alloy steel tubes. Singapore: Springer Singapore; 2021. p. 153–64.
12. Roy MJ, Klassen RJ, Wood JT. Evolution of plastic strain during a flow forming process. J Mater Process Technol. 2009;209(2):1018–25.
13. Guillot M, McCormack T, Tuffs M, Rosochowski A, Halliday S, Blackwell P. Shear forming of 304L stainless steel—microstructural aspects. Procedia Eng. 2017;207:1719–24.
14. Podder B, Mondal C, Ramesh Kumar K, Yadav DR. Effect of preform heat treatment on the flow formability and mechanical properties of AISI4340 steel. Mater Design. 2012;37:174–81.
15. Maj P, Adamczyk-Cieslak B, Lewczuk M, Mizera J, Kut S, Mrugala T. Formability, microstructure and mechanical properties of flow-formed 17–4 PH Stainless steel. J Mater Eng Perform. 2018;27(12):6435–42.
16. Nelson K, Conway A, Paslioglu K, Kulakov M, Milliken D. Analytical forming forces in two roller flow forming. Manuf Lett. 2024;43:18–26.
17. Niu PL, Li WY, Chen DL. Strain hardening behavior and mechanisms of friction stir welded dissimilar joints of aluminum alloys. Mater Lett. 2018;231:68–71.
18. Standard test methods for tension testing of metallic materials [Metric].
19. B. Beausir, J. Fundenberger, (2017) Analysis Tools for Electron and X-ray diffraction, ATEX-software, Université de Lorraine-Metz 2017
20. Rajan K, Deshpande P, Narasimhan K. Experimental studies on bursting pressure of thin-walled flow formed pressure vessels. J Mater Proc Technol—J Mater Process Technol. 2002;125:228–34.
21. Ebrahimi M, Tabei KH, Naseri R, Djavanroodi F. Effect of flow-forming parameters on surface quality, geometrical precision and mechanical properties of titanium tube. Proc Inst Mech Eng, Part E: J Process Mech Eng. 2018;232(6):702–8.
22. Rajan K, Narasimhan K. An investigation of the development of defects during flow forming of high strength thin wall steel tubes. Pract Fail Anal. 2001;1:69–76.

23. Singh AK, Kumar A, Narasimhan K, Singh R. Understanding the deformation and fracture mechanisms in backward flow-forming process of Ti-6Al-4V alloy via a shear modified continuous damage model. J Mater Process Technol. 2021;292:117060.
24. Gur M, Tirosh J. Plastic Flow Instability Under Compressive Loading During Shear Spinning Process. Journal of Engineering for Industry. 1982;104(1):17–22.
25. Zeng X, Fan XG, Li HW, Zhan M, Li SH, Wu KQ, Ren TW. Heterogeneous microstructure and mechanical property of thin-walled tubular part with cross inner ribs produced by flow forming. Mater Sci Eng, A. 2020;790:139702.
26. Miura H, Ito M, Yang X, Jonas JJ. Mechanisms of grain refinement in Mg–6Al–1Zn alloy during hot deformation. Mater Sci Eng, A. 2012;538:63–8.
27. Banerjee A, Wylie A, Da Silva L. Near-net shape manufacture of ultra-high strength maraging steel using flow forming and inertia friction welding: experimental and microstructural characterization. J Manuf Sci Eng. 2022;145(2):021004.
28. Wang XX, Zhan M, Fu MW, Gao PF, Guo J, Ma F. Microstructure evolution of Ti-6Al-2Zr-1Mo-1V alloy and its mechanism in multi-pass flow forming. J Mater Process Technol. 2018;261:86–97.
29. Naik SN, Walley SM. The Hall-Petch and inverse Hall-Petch relations and the hardness of nanocrystalline metals. J Mater Sci. 2020;55(7):2661–81.
30. Banerjee A, Ntovas M, Da Silva L, Rahimi S, Wynne B. Inter-relationship between microstructure evolution and mechanical properties in inertia friction welded 8630 low-alloy steel. Arch Civil Mech Eng. 2021;21(4):149.
31. Lee DN, Jeong H-T. The evolution of the goss texture in silicon steel. Scripta Mater. 1998;38(8):1219–23.
32. Kim JK, Lee DN, Koo YM. The evolution of the Goss and Cube textures in electrical steel. Mater Lett. 2014;122:110–3.
33. Shimizu Y, Ito Y, Iida Y. Formation of the Goss orientation near the surface of 3 pct silicon steel during hot rolling. Metall Trans A. 1986;17(8):1323–34.
34. Tsivoulas D, da Fonseca JQ, Tuffs M, Preuss M. Measurement and modelling of textures in flow formed Cr-Mo-V steel tubes. Mater Sci Eng, A. 2017;685:7–18.
35. Fonda RW, Knipling KE. Texture development in friction stir welds. Sci Technol Weld Joining. 2011;16(4):288–94.

Publisher's Note Springer Nature remains neutral with regard to jurisdictional claims in published maps and institutional affiliations.

Authors and Affiliations

Amborish Banerjee[1] · Kyle Nelson[1] · David Milliken[2] · Laurie da Silva[1]

✉ Amborish Banerjee
amborish.banerjee@strath.ac.uk; amborishbanerjee1205@gmail.com

[1] Advanced Forming Research Centre (AFRC), University of Strathclyde, 85 Inchinnan Drive, Inchinnan, Renfrewshire PA4 9LJ, UK

[2] Boeing Research and Technology—Europe, 85 Inchinnan Drive, Renfrew PA4 9LJ, UK